FULL PAPER

Phase Transformations and Structural Developments in the Radular Teeth of *Cryptochiton Stelleri*

*Qianqian Wang, Michiko Nemoto, Dongsheng Li, James C. Weaver, Brian Weden, John Stegemeier, Krassimir N. Bozhilov, Leslie R. Wood, Garrett W. Milliron, Christopher S. Kim, Elaine DiMasi, and David Kisailus**

During mineralization, the hard outer magnetite-containing shell of the radular teeth of *Cryptochiton stelleri* undergoes four distinct stages of structural and phase transformations: (i) the formation of a crystalline α-chitin organic matrix that forms the structural framework of the non-mineralized teeth, (ii) the templated synthesis of ferrihydrite crystal aggregates along these organic fibers, (iii) subsequent solid state phase transformation from ferrihydrite to magnetite, and (iv) progressive magnetite crystal growth to form continuous parallel rods within the mature teeth. The underlying α-chitin organic matrix appears to influence magnetite crystal aggregate density and the diameter and curvature of the resulting rods, both of which likely play critical roles in determining the local mechanical properties of the mature radular teeth.

Q. Wang, Dr. M. Nemoto, Dr. D. Li,
G. W. Milliron, Prof. D. Kisailus
Department of Chemical
and Environmental Engineering
University of California
Riverside, CA 92521, USA
E-mail: david@engr.ucr.edu
Dr. J. C. Weaver
Wyss Institute for Biologically Inspired Engineering
Harvard University
Cambridge, MA 02138, USA
B. Weden, L. R. Wood
Materials Science and Engineering Program
University of California
Riverside, CA 92521, USA
J. Stegemeier, Prof. C. S. Kim
School of Earth and Environmental Sciences
Chapman University
One University Drive
Orange, CA 92866, USA
Dr. K. N. Bozhilov
Central Facility for Advanced Microscopy
and Microanalysis
University of California
Riverside, CA 92521, USA
Dr. E. DiMasi
National Synchrotron Light Source
Brookhaven National Laboratory
Upton NY 11973, USA

DOI:10. 1002/adfm.201202894

1. Introduction

Through diversification and specialization, biological systems have evolved a wide range of complex hierarchically ordered structural materials that often exhibit superior mechanical properties compared to their anthropogenic counterparts.[1] One such example is found in the heavily mineralized and abrasion-resistant radular teeth of the chitons, a group of elongated herbivorous mollusks that are protected dorsally by eight overlapping shell plates. The chitons graze for algae on hard substrates using a specialized rasping organ called the radula (**Figure 1**),[2–4] a conveyor belt-like structure located in the mouth (Figure 1A) that contains numerous parallel rows of mineralized teeth. During the feeding process, the first few rows of teeth at the anterior end of the radula are involved in grazing and become worn. New teeth are continuously produced at the posterior end of the radula and enter the wear zone at the same rate at which teeth in the anterior-most row are shed from the growing ribbon.[5,6]

The Gumboot Chiton, *Cryptochiton stelleri*, a common inhabitant of the rocky shores of the temperate Northeastern Pacific, is the world's largest species of chiton, reaching a maximum length of more than 30 cm (Figure 1B,C).[2–4] The radula of *C. stelleri* contains more than 70 rows of mineralized and curved tricuspid teeth (Figure 1D). The fully mineralized radular teeth consist of an iron phosphate/magnetite core-shell structure that displays remarkable mechanical properties including the highest reported hardness and modulus of any known biomineral.[7] The organic matrix of these teeth consists primarily of α-chitin (a polymer of β-1, 4-linked N-acetylglucosamine units) and provides a three-dimensional structural framework onto which the mineral phases are precipitated. The resulting mature teeth exhibit a decreasing hardness and modulus from the leading to trailing tooth edges and due to the resulting asymmetrical wear patterns, create a self-sharpening condition.[6] This design affords the teeth the ability to withstand abrasion, impact, and fatigue during substrate rasping events, similar to conditions experienced by industrial machinery such as tunnel boring, oil drilling, shaping, and machining tools.[6] Since every stage of tooth development is contained within a single radula (Figure 1E), it thus provides an ideal model system

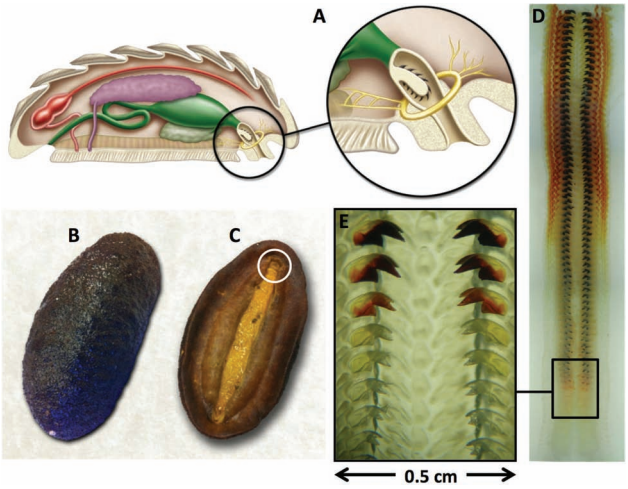

Figure 1. Chiton anatomy and gross morphological features of the radular teeth. A) Diagrammatic lateral view of a representative chiton body plan, B) dorsal and C) ventral views of *Cryptochiton stelleri* (in this species, the characteristic overlapping shell plates shown in A are internal and thus not visible in the photo). The location of the mouth (which contains the radula) is circled in white. D) Optical micrograph of an entire radula from *C. stelleri*, containing more than 70 rows of parallel mineralized teeth. E) Transitional zone near the posterior end of the radula demonstrating a gradual change in tooth color from transparent to black, representing the earliest stages of mineralization.

for investigating the dynamic processes of biomineralization during tooth growth and maturation.[8–13]

The radular teeth of *C. stelleri* were first studied by Lowenstam in the 1960s, who identified the presence of ferritin, in both crystalline and paracrystalline phases, as a likely shuttling vehicle for iron during tooth mineralization.[14] Lowenstam further showed that an open framework organic matrix was present in non-mineralized teeth and likely acted as a template for mineral deposition and in 1979, Kirschvink and Lowenstam confirmed that during the earliest stages of mineralization in the outer margins of the teeth of *C. stelleri,* ferrihydrite was first precipitated and was later transformed to magnetite.[15,16] However, in these early studies, the magnetite mineral phase was assumed to be approximately homogeneous throughout the shell region and nothing was known regarding the gradient in mechanical properties from the leading to trailing edge of the teeth, which was only recently described.[17] In light of these new observations, and to help clarify how the dynamics of tooth mineralization can influence their regio-specific mechanical properties, we report here an interdisciplinary study into the sequential stages of radular tooth mineralization in *C. stelleri* using synchrotron X-ray diffraction (XRD), synchrotron micro-X-ray fluorescence (μ-XRF), transmission electron microscopy (TEM) and scanning electron microscopy (SEM).

2. Results

2.1. Ultrastructure of the Mature Radular Tooth

SEM analyses of longitudinally fractured surfaces from mature teeth from *C. stelleri* (**Figure 2**) reveal a regionally segregated composite core-shell structure. Outside of the iron phosphate core region of the tooth is the shell region consisting of either magnetite particles or rods, whose longitudinal axes are oriented relative to curvature of the tooth's surface. From the leading edge of a tooth to its trailing edge, there are four distinct morphological transitions in the magnetite phase (Figure 2): (i) surrounding the entire periphery of each tooth is a very thin zone of condensed magnetite nanoparticles, which is thickened to a width of up to 2 µm at the outermost surface of the leading edge, (ii) beneath this thin granular veneer are bundles of magnetite rods oriented parallel to the leading edge of the tooth, (iii) these rods then undergo a gradual bending around the iron phosphate core until, (iv) their orientation becomes once again parallel with the trailing edge of the tooth. SEM measurements of the magnetite rods from these specific regions reveal an increase in rod diameter from the leading edge (162 ± 22 nm) to the trailing edge (194 ± 30 nm) of the tooth which is correlated

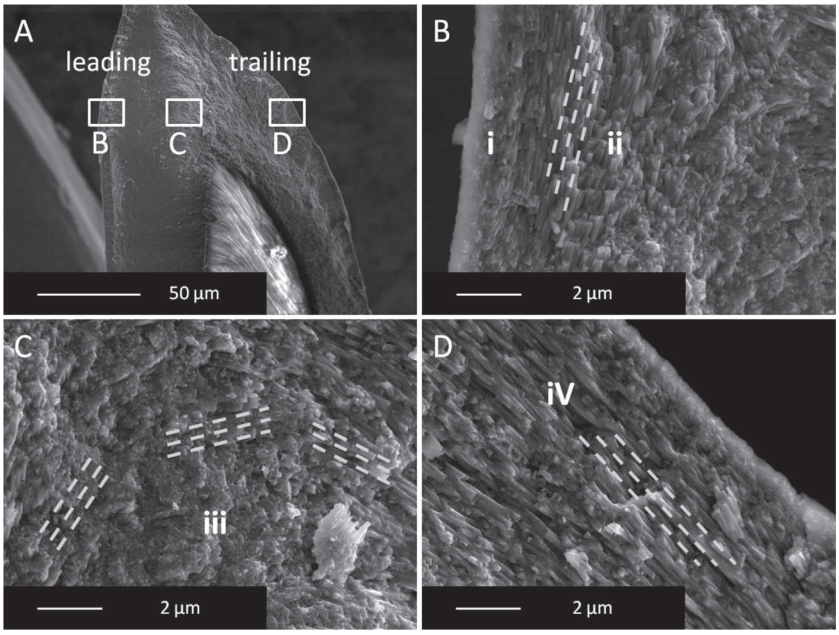

Figure 2. Magnetite structural diversity at the apex of a fully mineralized radular tooth from *C. stelleri*. A–D) Scanning electron micrograph of a longitudinal fracture surface of a mature radular tooth showing the iron phosphate core (lighter) and the magnetite shell region (darker). Regional structural heterogeneity includes (i) the granular magnetite veneer, the magnetite rods oriented parallel to the (ii) leading and (iv) trailing tooth edges and (iii) a gradual bending at transitional zone between them. The dashed lines illustrate the prevalent orientation of the rods in regions (ii), (iii), and (iv).

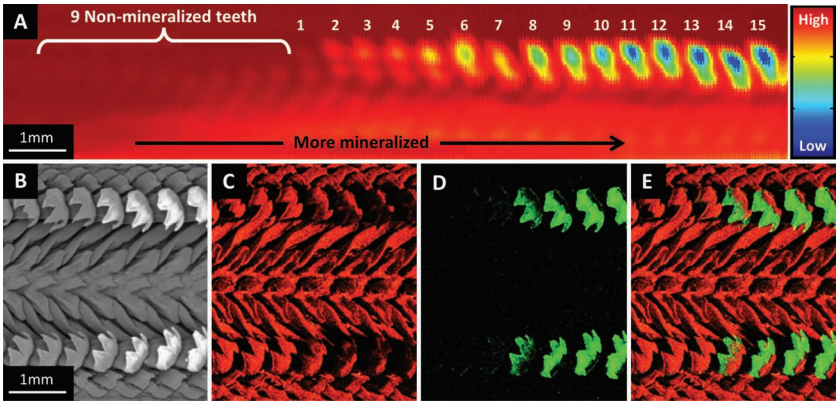

Figure 3. Early stages of radular tooth mineralization. A) Synchrotron X-ray transmission map (lateral view) of 24 partially mineralized radular teeth (still attached to the basal ribbon) reveals a gradual increase in electron density from the posterior to the anterior regions, corresponding to an increase in the extent of mineralization. B) Plan-view back-scattered scanning electron microscopy (BS-SEM) and energy dispersive spectroscopy (EDS) highlighting C) carbon, D) iron, and E) carbon-iron distribution during the transition from the nonmineralized to partially mineralized state.

with a significant decrease in hardness and modulus throughout the same region.[17]

2.2. Phase Transformations

Progressive mineralization in the immature teeth was revealed though synchrotron X-ray transmission mapping, Energy dispersive spectroscopy (EDS) mapping, and backscattered scanning electron microscopy (BS-SEM). A sequential decrease in X-ray transmittance through a set of 24 immature radular teeth (still attached to the basal membrane via their nonmineralized stalk) of *C. stelleri* suggests a gradual increase of mineral content (**Figure 3**A), an observation further supported by BS-SEM and EDS analysis (Figure 3B–E) with mineralization first occurring in the leading edges of the teeth.

For all subsequent analyses discussed in this report, the teeth will be numbered sequentially, referenced from the earliest visible signs of mineral deposition (which we will call "Tooth #1"). This tooth is easily identifiable with optical microscopy as the first tooth to change from transparent to yellow (the third tooth from the bottom in Figure 1E), and is the first tooth to contain levels of iron detectable with EDS.

To study phase transformations in the radular teeth at this early stage of development, synchrotron X-ray diffraction mapping in transmission geometry with a 100-µm step size (and a 100-µm spot size) was performed along the entire radula, with comparison measurements made against magnetite, α-chitin, and ferrihydrite reference standards. Four representative diffraction frames (**Figure 4**) from (A) nonmineralized teeth, (B) tooth #1, (C) tooth #3, and (D) tooth #5 provide snapshots of the early stages of the mineralization process. Integrated XRD patterns plotted as Intensity vs Q ($Q = 2\pi/d$) from these frames allow us to discern the presence of multiple mineral phases within each tooth (**Figure 5**A). Based on the comparison of representative plots from radular teeth and mineral standards (**Table 1**), α-chitin is the only crystalline phase detected in the nonmineralized teeth and persists throughout all of the examined teeth. Six-line ferrihydrite appears in tooth #1 and persists until tooth #5. Magnetite is first detected in tooth #2 and is observed in all subsequent teeth. The only crystalline mineral detected in tooth #5 is magnetite, which indicates the end point of the large scale iron oxide phase transformation (Figure 4).[18–20]

To investigate the compositional change from ferrihydrite to magnetite with increasing

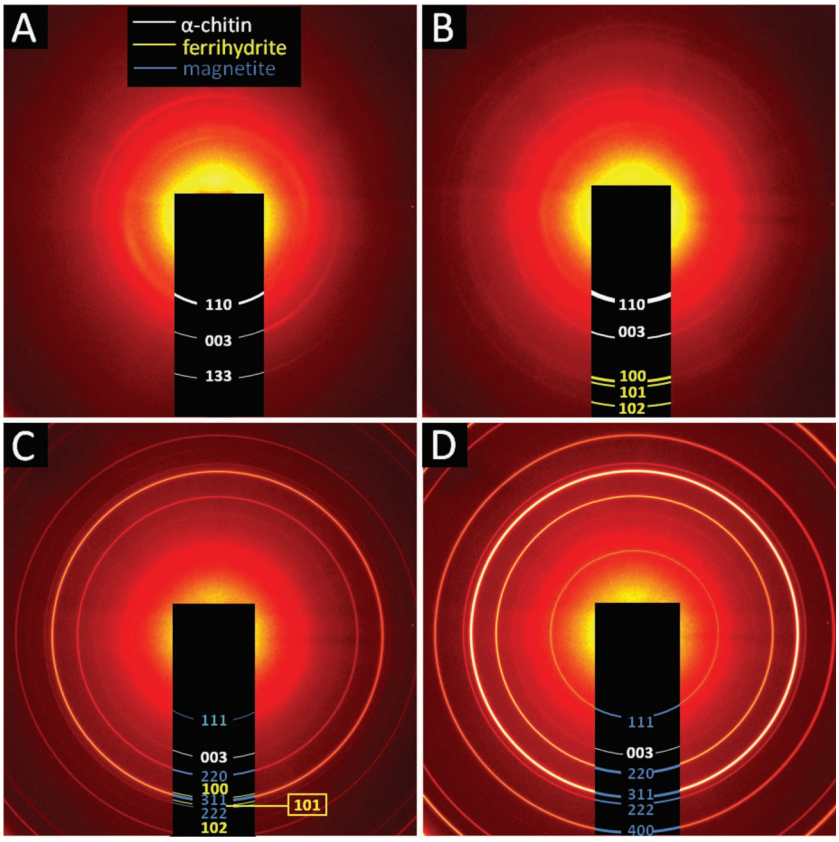

Figure 4. Representative synchrotron X-ray diffraction frames from A) nonmineralized teeth, B) tooth #1, C) tooth #3, and D) tooth #5 revealing the transformation from ferrihydrite to magnetite during the early stages of radular tooth mineralization. Miller indices of each phase are labeled on the frames. White, yellow and blue arcs correspond to α-chitin, ferrihydrite and magnetite, respectively and are indexed from the azimuthally integrated patterns shown in Figure 5A.

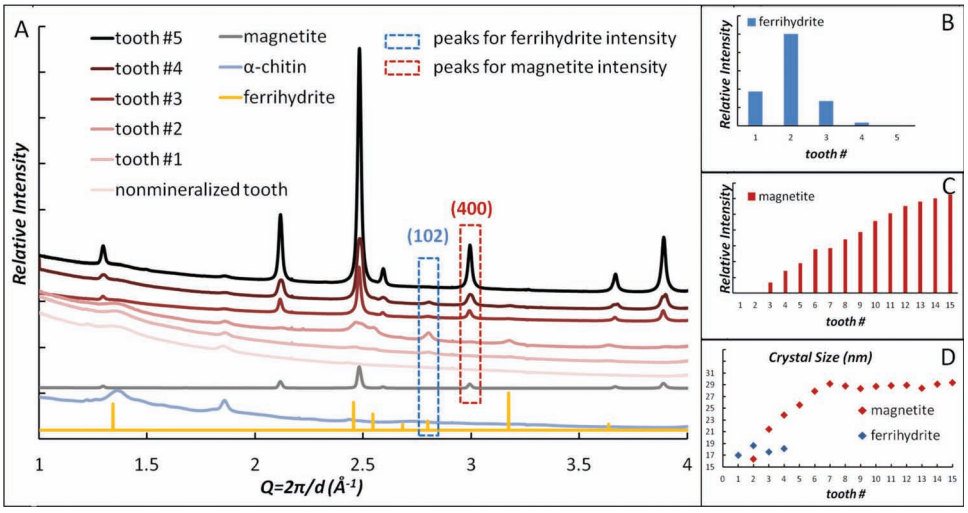

Figure 5. Qualitative phase transformations during the early stages of radula mineralization. (A) Representative diffracted X-ray intensity vs Q (Q = 2π/d) plots from azimuthally integrated patterns such as those shown in Figure 4. Spectra show powder diffraction patterns from a nonmineralized tooth; teeth #1, #2, #3,and #5; magnetite and α-chitin standards, and a ferrihydrite literature reference.[20] Diffraction peaks Q = 2.802 $Å^{-1}$ (specific to the 102 ferrihydrite reflection) and Q = 2.991 $Å^{-1}$ (specific to the 400 magnetite reflection) were fit to obtain the tooth-dependent integrated reflection areas and the full-width at half-maximum. The intensity of (B) ferrihydrite and (C) magnetite are represented by the integrated peak areas. (D) The change of the average crystal size of magnetite and ferrihydrite were calculated from the full-width at half-maximum of representative reflections via the Scherrer equation.

tooth maturation, peaks at Q = 2.802 $Å^{-1}$ (specific to the (102) reflection of ferrihydrite) and at Q = 2.991 $Å^{-1}$ (specific to the (400) reflection of magnetite) were analyzed separately. Polynomial and Lorentzian functions were applied to fit the Intensity vs. Q plots for the selected reflections. The area under each curve was obtained and used as a metric to quantify the corresponding mineral phases (Figure 5B,C), while the full-width at half-maximum values of the ferrihydrite (102) and magnetite

Table 1. Q ($Å^{-1}$) values derived from diffraction peaks in Figure 5A.

α-chitin(standard)	ferrihydrite [20]	magnetite (standard)	nonmineralized tooth	tooth #1	tooth #3	tooth #5
1.216						
1.256			1.220	1.231	1.231	1.231
		1.297			1.297	1.297
	1.341			1.347	1.347	
1.360			1.364			
1.854			1.858	1.858	1.858	1.858
		2.115			2.115	2.115
2.434			2.449			
	2.455			2.461	2.465	
		2.479			2.492	2.479
	2.545			2.551	2.546	
		2.591			2.591	2.591
	2.682			2.690	2.667	
	2.798			2.802	2.802	
		2.991			2.991	2.991
	3.173			3.175	3.175	
	3.636			3.634	3.634	
		3.665			3.665	3.665
		3.890			3.890	3.890

(400) reflections were obtained and used as a metric to quantify the size of the corresponding crystals (Figure 5D). The compiled results were averaged from the integrated peak areas from the 10 point locations on each tooth that corresponded to the highest X-ray absorbance. From these measurements, it was determined that ferrihydrite concentration reaches a maximum in tooth #2, decreasing to about 1/3 of the maximum concentration in tooth #3, and disappearing entirely by tooth #5 (Figure 5B). In contrast, magnetite peak intensity, which first appears in tooth #2, increases steadily for the next 20+ teeth (Figure 5C) until finally reaching a stable maximum throughout the remaining radular teeth. From Scherrer analyses of the corresponding diffractograms, no pronounced change in ferrihydrite crystal size was observed (average size of ferrihydrite crystals varied from 17 to 18.7 nm from tooth #1 to #4) during the early stages of tooth mineralization. In contrast, magnetite crystals initially observed in tooth #2 (with a 16.4 nm crystal diameter), continuously grew to 29.2 nm (tooth #7), with no subsequent growth thereafter (Figure 5D).

In order to spatially resolve the phase transformations in the radular teeth of *C. stelleri* with more accuracy, synchrotron μXRF (**Figure 6**) was performed on radular teeth #1-4 using a 2.5 × 2.5 μm beam spot size (1600 times smaller than that used for the XRD analysis). Principal component analysis (PCA) was then applied to the multiple Fe μXRF maps, resulting in two principal component maps which were correlated with the concentrations of total iron (Figure 6A) and ferrous iron (Figure 6B) in each tooth. The resulting PCA maps indicated that the concentrations of both total iron and ferrous iron increase with tooth maturity. Furthermore, from a comparison of the PCA maps, the presence of ferric iron can be inferred wherever total iron is present and ferrous iron is absent. Accordingly, ferric iron appears to be prevalent across the entire tooth surface, including the interface between each tooth and its base, while ferrous iron first appears at the tip of tooth #2 and then propagates along the leading edge with increasing tooth maturation.

Based on synchrotron XRD analyses, the ferrous and ferric iron identified by μXRF/PCA can be assigned to magnetite and ferrihydrite, respectively. To more clearly distinguish between the two species, several (2–5) discrete points per radular tooth were selected using the PCA maps for micro X-ray absorption near edge structure (μXANES) analysis.[21] From the resulting μXANES spectra, the two spectra exhibiting the greatest differences in the Fe K-edge position (a proxy for oxidation state) were selected as end members to represent the most ferric and ferrous locations among all four teeth. The Fe K-edge multiple energy (ME) μXRF maps were then fitted in a non-negative linear least-squares format using normalized fluorescence values obtained from the two end member μXANES spectra corresponding to the five different map energies, similar to the method applied by Mayhew et al.[22] The resulting manually scaled two-color map shows the increasing abundance of a ferric (ferrihydrite) phase across the surface of the radular teeth and the evolution of a more ferrous (magnetite) phase along the leading edge (Figure 6C), consistent with the results of the PCA analysis.

Based on the synchrotron μXRF analysis, both the ferrihydrite deposition and the phase transformation to magnetite initiate at the tip of the leading edge of the tooth.

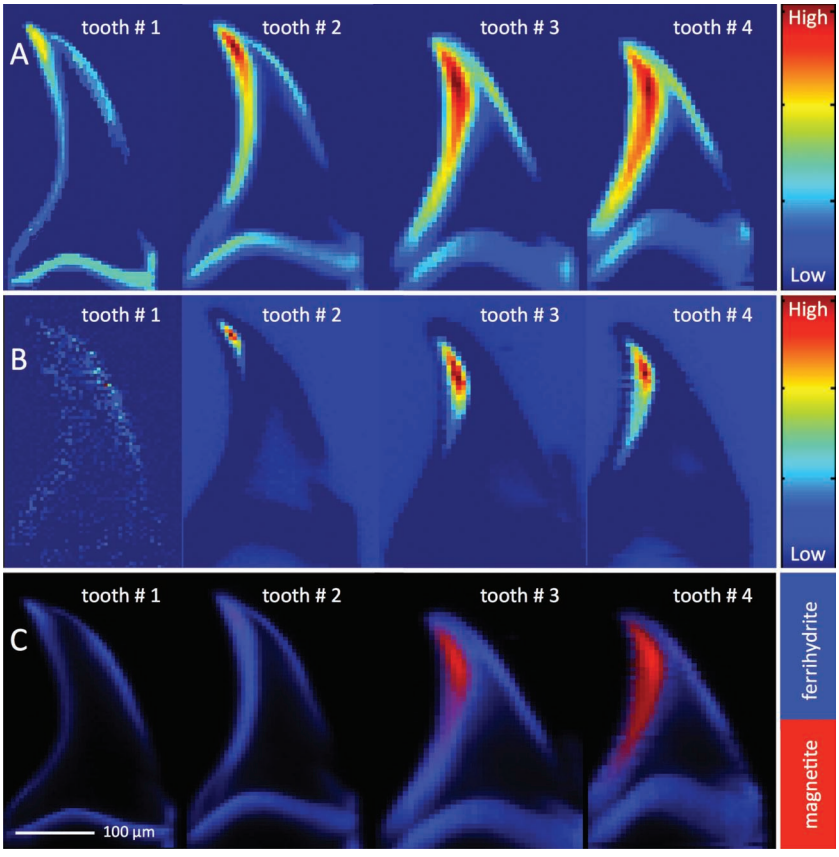

Figure 6. Micro X-ray fluorescence (μXRF) analysis of longitudinal thin sections of radular teeth #1–4 from C. stelleri reveals the local iron oxide transformation. Both the intensity of A) total iron and B) ferrous iron increase across the leading edge with increasing tooth maturation. C) Micro X-ray absorption near edge structure (μXANES) analysis reveals an increasing abundance of magnetite across the shell region along the leading edge of radular teeth.

2.3. Structural Development

The magnetite rod formation process, including the organic matrix-mediated mineral aggregation and growth, was further investigated using SEM and TEM.

To understand the process of magnetite nanorod formation, this dynamic structural transformation was studied by analyzing the fracture surfaces from the tips of teeth #1 through #4 with SEM (**Figure 7**). An increase of mineral crystal aggregate size coupled with a decrease in the diameter of surrounding fibrillar organic matrix was found with increasing tooth maturation. Crystal aggregates measuring 41 ± 6 nm in diameter begin to nucleate along the closely packed fibers at

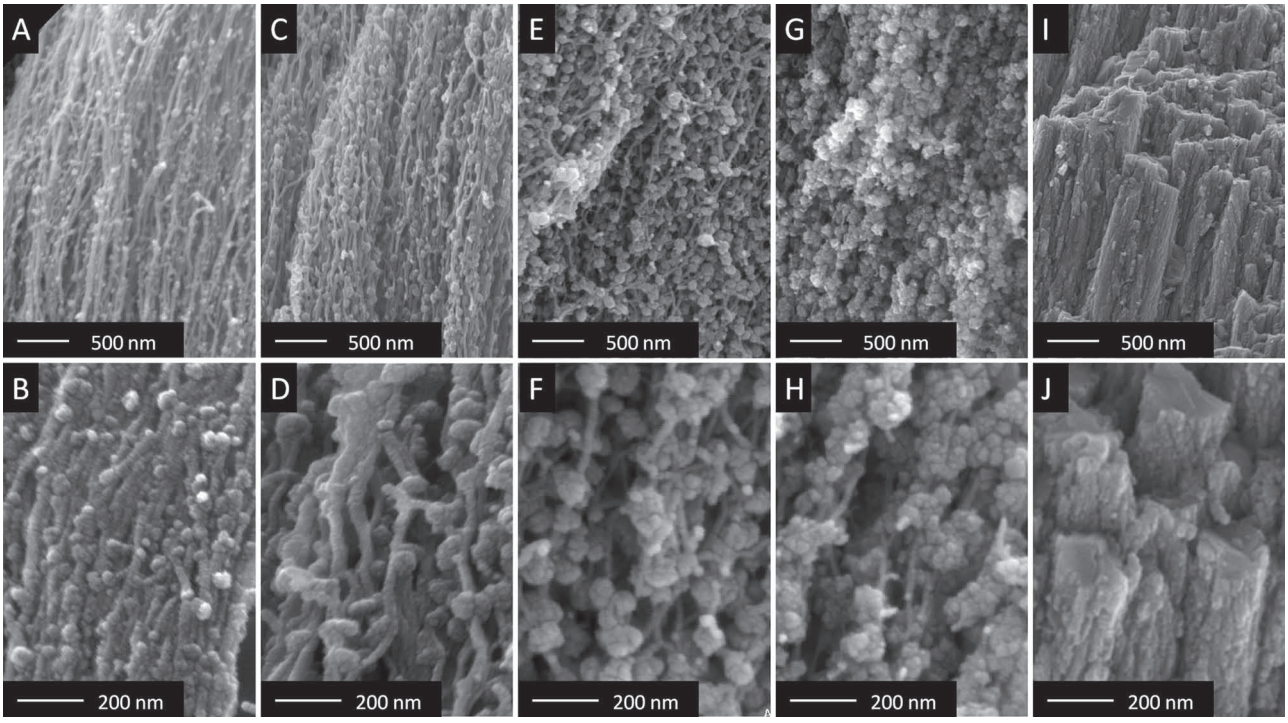

Figure 7. Sequential stages of magnetite rod formation during radular tooth maturation. Scanning electron microscopy analyses of fracture surfaces from the tips of A,B) tooth #1, C,D) tooth #2, E,F) tooth #3, G,H) tooth #4 and I,J) a fully mineralized tooth.

the tip of tooth #1 (Figure 7A,B), the location at which BS-SEM, TEM, and EDS data indicate that mineral is first deposited. The size of the aggregates in the same tooth region increases dramatically to 74 ± 10 nm in tooth #2 (Figure 7C,D), where the phase transformation from ferrihydrite to magnetite is initiated (as revealed by XRD and μXRF). The aggregates continue to grow from 90 ± 11 nm in tooth #3 (Figure 7E,F) to 107 ± 18 nm in tooth #4 (Figure 7G,H), finally forming 171 ± 20 nm diameter continuous rods in the fully mineralized teeth (Figure 7I,J). Additionally, the diameters of the organic matrix fibers decrease from 37 ± 2 nm in tooth #1 to 20 ± 3 nm in tooth #4 and are indistinguishable under SEM in the fully mineralized teeth.

TEM analyses of the tip, middle, and bottom sections through the shell region of tooth #3, as well as the tip of tooth #5 (**Figure 8**A), were investigated to look for any regional differences in solid-state phase transformations and aggregation during tooth formation. In tooth #3, mineral deposition occurs on the fibrillar organic matrix in all three sections (Figure 8B–D). A representative high resolution TEM micrograph from the trailing edge of the tip reveals that each aggregate consists of 16-19 nm crystallites that are in direct contact with the organic matrix fibers, suggesting their potential nucleating properties (Figure 8E), an observation consistent with the templating activity of the chitinous organic matrix described from other chiton species.[23] Analyses of the tooth leading edge, from the tip (Figure 8B), middle (Figure 8C) and bottom (Figure 8D), reveal a decrease in aggregate size and an increase in crystal aggregate density. Along the leading edge, the average mineral aggregate size is 175.0 ± 24 nm at the tip, 70.7 ± 14 nm at the middle, and 40.5 ± 8 nm at the base. The aggregate density (number of aggregates per unit area) is 6.4/μm^2 at the tip, increasing to 66.9/μm^2 at the middle, and 106.2/μm^2 at the bottom. Selected area electron diffraction (SAED) reveals that the crystal aggregates at the tip of this tooth consist of ferrihydrite and magnetite, while the ones at the bottom contain only ferrihydrite.

At the tip of tooth #3, TEM reveals a decrease of crystal aggregate size and an increase in crystal aggregate density from the trailing edge to the leading edge is revealed concurrently with a decrease of the spacing between fibers of the organic matrix (Figure 8B,F). The average spacing between fibers at the tip of the trailing edge is 116 ± 35 nm, which is larger than those at the leading edge (106 ± 24 nm). At the tip of the trailing edge, the crystal aggregate size is 211.0 ± 29 nm and crystal aggregate density is 2.6/μm^2 (Figure 8F).

Analysis of the tip of tooth #5 reveal that the mineral aggregates increase to ≈300–400 nm in size and SAED from this region confirms the sole presence of magnetite (Figure 8G). High-resolution TEM imaging (Figure 8H) and convergent beam electron diffraction (CBED) (Figure 8H$_{1,2}$) of these magnetite aggregates demonstrate the presence of a core consisting of multiple nanocrystallites (16–19 nm) surrounded by larger (56–128 nm) crystals.

3. Discussion

Based on the initial findings of Towe and Lowenstam,[16] who demonstrated the formation of a crystalline α-chitin organic matrix that forms the structural framework

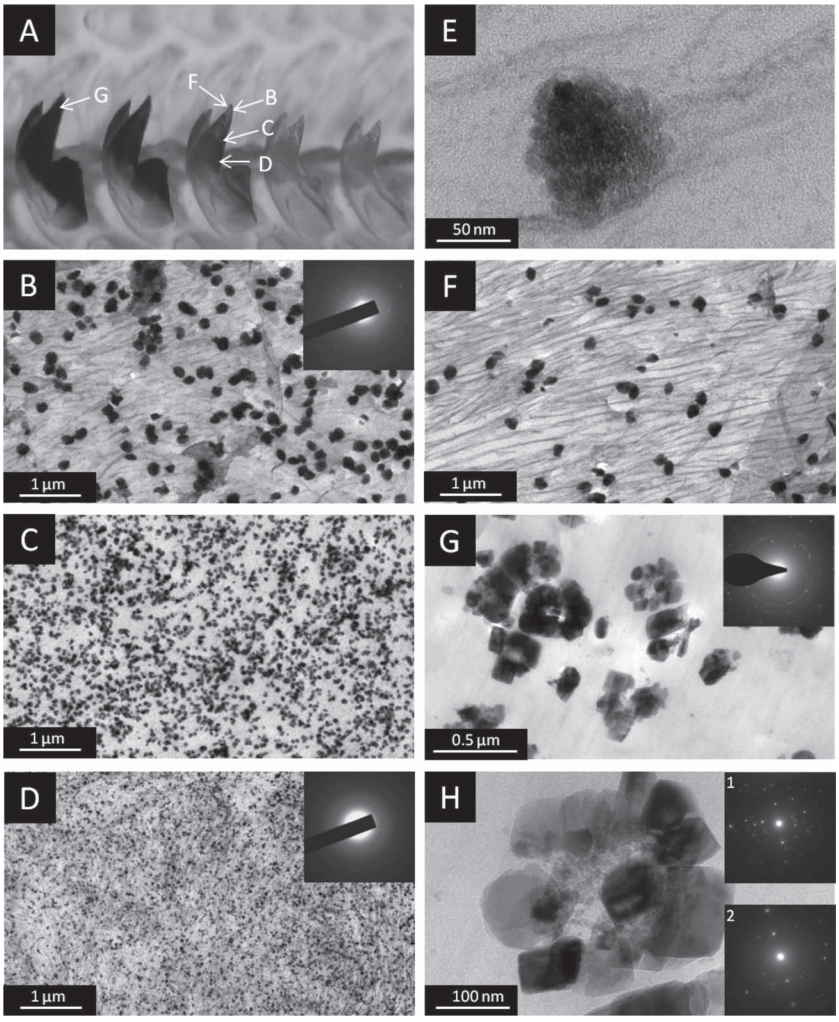

Figure 8. Transmission electron microscopy (TEM) analyses of phase transformations during early radular tooth mineralization (i.e., teeth #3 and #5). A) An optical micrograph illustrates the locations of TEM sections. At the leading edge of tooth #3, there is a progressive increase in crystal aggregate density and a corresponding decrease in crystal aggregate size from B) the tip to C) the middle and D) the base of each tooth. Selected area electron diffraction (SAED) reveals the presence of ferrihydrite and magnetite at the tooth tip, while the nanocrystalline aggregates at the base only contain ferrihydrite. E) Deposited mineral at the trailing edge of the tip of the tooth is physically contacted with the fibrillar organic matrix and consists of aggregated nanocrystallites measuring 16–19 nm in diameter. F) The trailing edge of the tip of tooth #3 has a lower crystal aggregate density and larger crystal aggregate size together with higher spacing between organic fibrils. G,H) Magnetite crystal aggregates from the tip of tooth #5 consist of multiple nanocrystallites with 16–19 nm in size, surrounded by larger single crystals of magnetite. Convergent beam electron diffraction (CBED) illustrates that both the (H_1) 16–19 nm crystals in the cores of the crystal aggregates and the (H_2) larger domains along their perimeter are single magnetite crystals.

of the non-mineralized teeth, our results reveal that the hard outer magnetite containing shell of the radular teeth of *C. stelleri* forms via a series of structural and phase transformations: (i) the templated synthesis of ferrihydrite crystal aggregates along the preformed chitinous organic matrix, (ii) aggregation of the crystal aggregates with a subsequent solid state phase transformation from ferrihydrite to magnetite, and (iii) progressive magnetite crystal growth to form continuous parallel rods within the mature teeth.

3.1. Phase Transformation

Our study demonstrates that α-chitin (which is easily distinguished from the β and γ forms by XRD)[24] is the only crystalline organic phase produced in the teeth of *C. stelleri*, confirming Towe and Lowenstam's speculation regarding the identity of chitin-like organic fibers in the early stages of radular tooth development.[16]

Although α-chitin may act as a universal template in biomineralization that can induce the formation of many minerals,[25] it is not strongly implicated for the selection of iron ions as it is also found in biominerals devoid of iron oxides, such as the calcified exoskeletons of crustaceans.[26] In addition, α-chitin alone does not necessarily control the initial phase of the precipitated minerals since goethite is found to be the initial mineral phase that forms on the chitin fibers within the radular teeth of limpets.[27] It therefore seems reasonable that it is the chitin-associated proteins that are primarily responsible for the specific mineral nucleation, growth, and phase transformations within the radular teeth.[10]

Kim et al. presumed that the iron transported into the radular teeth of the chiton *Acanthopleura hirtosa* was Fe(II), which then oxidized to form ferrihydrite.[13] However, our µXRF data provides evidence that ferrous iron is present after deposition of ferric iron. Therefore, the suggested redox mechanism of ferrihydrite formation in *Acanthopleura hirtosa* does not likely apply to the radular teeth of *C. stelleri*. Since the temperature of the natural habitat of *C. stelleri* is ≈15 °C, we propose that ferric iron hydrolyzes in water and forms positively charged ferric iron hydroxides.[28–35] Due to the low solubility of Fe(III) compounds at pH values similar to that of seawater, super saturation with respect to ferrihydrite solubility can rapidly occur, resulting in the spontaneous precipitation of metastable ferrihydrite. Since the Gibbs free energy of ferrihydrite formation is comparable to other iron oxides like goethite (α-FeO(OH)), lepidocrocite (γ-FeO(OH)), or akaganeite (β-FeO(OH)), and the surface enthalpy of hydrous phases are lower than that of anhydrous ones, it is not surprising that the first mineral phase appearing in radular teeth is ferrihydrite.[36]

Synchrotron analyses of the radular teeth identify a phase transformation from ferrihydrite to magnetite initiating at tooth #2. The highly hydrolyzed nanocrystalline ferrihydrite, with active adsorption sites on its surface, tends to transform to thermodynamically more stable phases, including magnetite. This transformation from ferrihydrite to magnetite is thought to occur via the absorption of ferrous iron ions.[37–40]

Synchrotron microdiffraction and TEM analyses of teeth #1–#4 confirmed the presence of ferrihydrite with an average crystallite diameter of ≈17–19 nm and no ferrihydrite crystal growth was observed within these teeth. Furthermore, synchrotron microdiffraction revealed the initial formation of magnetite in tooth #2 with crystallite diameters of 16.4 nm, dimensions similar to those observed in the ferrihydrite domains.

By tooth #5, magnetite was the only mineral phase detected. TEM observations of this tooth (i.e., #5) revealed magnetite crystal aggregates consisting of a core with 16–19 nm nanocrystals, similar to those found in the ferrihydrite-based crystal aggregates in less mature teeth. This is consistent with a solid-state phase transformation from ferrihydrite to magnetite seen in the iron reducing bacteria, *Shewanella putrefaciens*.[38] Similarly, it was suggested that adsorption of Fe^{2+} to ferrihydrite (or ferric hydroxide; i.e., very short range ordered hydrated iron oxohydroxides) in wholly synthetic systems induced a solid-state transformation with no change in crystallite size.[39] In addition, subsequent decreases in the concentration of ferrous iron were shown to induce crystal growth of magnetite in synthesized suspensions of ferrihydrite.

Our TEM analyses have revealed that the magnetite crystal aggregates in tooth #5 had significantly larger crystallites (≈56–128 nm) of magnetite on the perimeter of the crystal aggregates, indicating significant grain growth, while the size of core magnetite crystals in these aggregates remained unchanged. Recently, we conducted proteomic analysis of the fully mineralized radular teeth from *C. stelleri* and identified several proteins and peptides that specifically existed in the mineralized zones of the teeth. One of these identified peptides, exhibited significant homology to the C-terminal domain of a peroxiredoxin-6-like protein.[40] This protein is known to act as an electron donor (i.e., reduction agent) in both eukaryotic and prokaryotic organisms.[42–44] In addition, the aldehyde ferredoxin-oxidoreductase gene that may contribute to ferric iron reduction has been identified in the magnetotactic bacterium, *Magnetospirillum magneticum*.[40] This observation suggests that proteins found in fully mineralized teeth may function to control the reduction of iron species and therefore control the initial phase transformation from ferrihydrite to magnetite by adsorption of Fe^{2+} ions with subsequent solid-state transformation.

3.2. Structural Development

The underlying α-chitin organic matrix appears to influence magnetite crystal aggregate density (number of aggregates per unit area) and the diameter and curvature of the resulting rods, all of which likely play critical roles in determining the local mechanical properties of the mature radular teeth.

All of the crystal aggregates (more than 100) observed in TEM were in physical contact with the organic fibrils (Supporting Information Figure 1), suggesting that ferrihydrite is synthesized de novo on the organic fibrils via heterogeneous nucleation. Based on our analyses of peptides extracted from the cusps of fully mineralized teeth of *C. stelleri*, a peptide similar to the iron binding protein, Mms6 was identified.[41,45,46] Previous studies have shown that a similar protein found in the teeth of *Acanthopleura hirtosa* is distributed on the organic matrix fibrils and is likely responsible for enhancing ferrihydrite mineral nucleation.[10,47] Here, we suggest that the α-chitin fibrils within the radular teeth of *C. stelleri* may be coated with an iron binding Mms6-like protein, which assists the mineralization process by attracting ferric ions. By increasing the local concentration of ferric iron (which has a low solubility at near-neutral pH) on these organic matrix fibers, heterogeneous nucleation of ferrihydrite can be induced.

Morphological investigations of the tip of tooth #3, from the trailing edge to the leading edge, revealed a decrease in crystal aggregate size and an increase of crystal aggregate density with a concurrent decrease in the spacing of the organic fibers. At the leading edge, fibers are more densely packed and thus we can expect a greater number of nucleation sites. In the trailing edge, the spacing between organic matrix fibers increases and thus, we expect fewer nuclei. In addition, there is a direct correlation between the organic fiber spacing on the leading and trailing edges of the non-mineralized radular teeth and the diameters of the corresponding magnetite rods in the mature teeth.

4. Conclusions

The results reported here detail the dynamic phase and microstructural transformations that occur during mineralization in the radular teeth of *C. stelleri*. Mineralization is initiated via the deposition of six-line ferrihydrite aggregates at the leading edge of the tooth tips. These aggregates subsequently transform to magnetite via a solid-state phase transformation, followed by magnetite crystal growth. These aggregates further form highly oriented rod-like elements that exhibit regionally defined geometries that depend on the periodic spacing of the surrounding organic matrix, and in turn, affect the regional mechanical properties of the mature teeth. These studies into the biomineralization processes in the radular teeth of *C. stelleri* thus illustrate several design principles that could be potentially applied to not only the biomimetic synthesis of iron oxides, but also the spatially confined template-directed growth of a wide range of inorganic crystal structures and structural ceramics with graded moduli.

5. Experimental Section

Research Specimens: Live specimens of *Cryptochiton stelleri* were collected from the temperate Eastern Pacific (Monterey, CA) and maintained in recirculating seawater system at 15 °C before use. Collection of *Cryptochiton stelleri* is permitted by the Department of Fish and Game and the California Natural Resources Agency. The radulae were dissected from these specimens and rinsed in fresh seawater to remove any loose organic debris.

Energy Dispersive Spectroscopy: For elemental mapping via EDS, 20 rows of immature teeth, centered on the site of initial mineral deposition and still attached to the basal ribbon were cut from an intact radula with a razorblade and then serially dehydrated to 100% ethanol. The tooth rows were then critical point dried with CO_2, mounted to conductive carbon tape and examined with a Tescan VEGA TS-5130MM SEM equipped with an IXRF Systems energy dispersive spectrometer. EDS mapping was performed at an accelerator voltage of 20 keV.

Synchrotron X-Ray Diffraction: 24 partially mineralized radular teeth (removed from the posterior end of the radula), still attached to the

basal ribbon, were cut from an intact radula with a razorblade and then serially dehydrated to 100% ethanol. The isolated teeth were then critical point dried with CO_2 and attached to a silicon wafer using conductive carbon tape. The radular teeth were transversely analyzed at beamline X6B of the National Synchrotron Light Source (NSLS) in Brookhaven National Laboratory using 19 keV X-rays and a beam spot focused to 100 μm × 100 μm. X-ray transmission mapping was performed on the entire sample using 1 s scans with a 50 μm step size to investigate the progressive change in electron density along the length of the radula. X-ray diffraction mapping was performed on the entire sample using a 100 s diffraction time with a 100 μm step size to reveal the crystalline phases present in the teeth. X-ray diffraction of reference standards, including α-chitin, magnetite, goethite, lepidocrocite and alumina was also performed using the same beamline settings. The synchrotron X-ray diffraction data were calibrated using an Al_2O_3 powder plate to determine camera parameters and subsequently the known *d*-spacing of magnetite were used to further refine sample-detector distance with radula patterns that contained strong magnetite peaks. This analysis was applied to all positions on the samples. The Datasqueeze software package (datasqueezesoftware.com) was used to calibrate and integrate the data. Intensity vs Q ($Q = 2\pi/d$) plots were integrated from the diffraction patterns and used for mineral phase analysis. Intensity vs 2θ plots were generated and selected reflections were fitted with polynomial and Lorentzian parameters to calculate the relative concentrations and crystal size of the specific mineral phases.

Synchrotron Micro X-Ray Fluorescence: Four partially mineralized teeth (#1, #2, #3 and #4) (still attached to the basal ribbon) were cut from an intact radula with a razorblade and fixed with gluteraldehyde (2.5%) in phosphate buffer for 2 h, followed by an overnight post fixation with OsO_4 (1%) at 4 °C. The sample was then serially dehydrated to 100% ethanol, embedded in Spurrs resin and cured for 24 h at 60 °C. The obtained resin block was sectioned with a diamond saw and polished in the longitudinal direction with silicon carbide grit paper to P1200 followed by polishing with diamond lapping films down to 0.25 μm. The result was a thin, finely polished specimen containing longitudinal cross sections of 4 partially mineralized teeth. μXRF imaging was performed on the polished sample at beamline 2-3 of the Stanford Synchrotron Radiation Lightsource (SSRL) using a Si (111) monochrometer detuned 20% at 7 keV and calibrated using Fe metal foil at 7112 eV. The sample was rastered across a 2.5 μm × 2.5 μm micro-focused X-ray beam and positioned at a 45° angle to the incident beam, with a 5 μm pixel step size and 125 ms dwell time per pixel. Multiple energy (ME) mapping was conducted near the Fe K-edge by rastering each line of the map at five discrete energies (7115, 7122, 7125, 7130, and 7140 eV) using a single element Vortex silicon drift detector (SII Nano Technology USA Inc.) situated perpendicular to the incident beam. These energies were selected based on XANES spectra of previously-collected model Fe compounds and chosen at points intended to maximize differences between ferrihydrite and magnetite. Principal component analysis (PCA) was conducted on the multiple energy Fe maps using the MicroAnalysis Toolkit (SMAK), yielding principal component maps which showed the spatial distribution of the dominant mineral phases which comprised the sample. These maps were in turn used to identify several (2–5) discrete points per radular tooth for micro X-ray absorption near edge structure (μXANES) analysis. All μXANES spectra were collected from 6880 to 7530 eV and then dwell time corrected, background-subtracted, and normalized for the incident X-ray beam intensity using the SIXPACK software package.[48]

Transmission Electron Microscopy: To investigate the early stages of magnetite mineralization, tooth #4 was cut from an intact radula with a razorblade and then fixed with gluteraldehyde (2.5%) in HEPES buffer (0.2M, pH7.2) for 2 h, followed by an overnight post-fixation with OsO_4 (1%) at 4 °C. The sample was then serially dehydrated to 100% ethanol, embedded in Spurrs resin and cured for 24 h at 60 °C in a microtome sample holder. 80 nm thick sections from several regions were microtomed from the resin block with a glass knife and imaged with a Tecnai T12 transmission electron microscope at 120 kV and a Philips/FEI CM300 operated at 300 kV.

Scanning Electron Microscopy: For fracture surface analyses, a single tooth still attached to the basal ribbon was cut from an intact radula with a razor blade, washed with DI water, fixed with 2.5% gluteraldehyde for two hours, and rinsed with DI water. The rows of teeth were then serially dehydrated to 100% ethanol and critical point dried with CO_2. Fracture surfaces of these dried teeth were created via impact with a razor blade and then mounted on an aluminum pin mount with conductive carbon tape. The samples were gold coated and then imaged with an FEI XL30 scanning electron microscope at 10 kV.

Statistical Analysis: The calculation of crystal aggregate size, organic matrix fiber spacing, and rod diameter were performed manually by measuring their dimensions directly from SE or TE micrographs. Approximately 50 measurements were acquired from each image and the means and standard deviations were determined. The crystal aggregate density in TEM images was obtained by dividing the total number of the crystal aggregates by the area of the corresponding image.

Supporting Information

Supporting Information is available from the Wiley Online Library or from the author.

Acknowledgements

Q.W. and M.N. contributed equally to this work. We thank Sara Krause for the illustration in Figure 1A, Dr. Kenneth Evans-Lutterodt of the National Synchrotron Light Source in Brookhaven National Laboratory for contributing his expertise at the microdiffraction endstation X13B, Dr. Vesna Stanic of the NSLS in BNL for her help in conducting experiments at the diffraction endstation X6B, and Dr. Sam Webb of Stanford Synchrotron Radiation Lightsource for his instrumental help with the μXRF measurements. The NSLS is supported under USDOE Contract DE-AC02-98CH10886. Portions of this research were carried out at the Stanford Synchrotron Radiation Lightsource, a Directorate of SLAC National Accelerator Laboratory and an Office of Science User Facility operated for the U.S. Department of Energy Office of Science by Stanford University. M.N. was supported, in part, by the JSPS International Training Program (ITP). We acknowledge the Central Facility for Advanced Microscopy and Microanalysis at UC Riverside for use of sample prep and electron microscopy imaging. This work was supported in part by ARO: W911NF-12-1-0257 and AFOSR: FA9550-12-1-0249.

Received: October 5, 2012
Published online: January 16, 2013

[1] B. L. Smith, T. E. Schaffer, M. Viani, J. B. Thompson, N. A. Frederick, J. Kindt, A. Belcher, G. D. Stucky, D. E. Morse, P. K. Hansma, *Nature* **1999**, *399*, 761.
[2] E. Ricketts, J. Calvin, *Between Pacific Tides*, 5th ed., Stanford University Press, Stanford **1985**.
[3] R. H. Morris, D. P. Abbott, E. C. Haderlie, *Intertidal Invertebrates of California*, Stanford University Press, Stanford **1980**.
[4] H. A. Lowenstam, S. Weiner, *On Biomineralization*, Oxford University Press, Oxford **1989**.
[5] J. A. Shaw, D. J. Macey, L. R. Brooker, *J. Mar. Biol. Assoc. U. K.* **2008**, *88*, 597.
[6] P. van der Wal, H. J. Giesen, J. J. Videler, *Mater. Sci. Eng., C* **2000**, *7*.
[7] M. F. Ashby, L. J. Gibson, U. Wegst, R. Olive, *Proc. R. Soc. London, Ser. A* **1995**, *450*, 123.
[8] C. W. Li, T. S. Chin, J. S. Li, S. H. Huang, *IEEE Trans. Magn.* **1989**, *25*, 3818.
[9] L. A. Evans, D. J. Macey, J. Webb, *Philos.Trans. R. Soc., B.* **1990**, *329*, 87.
[10] L. A. Evans, D. J. Macey, J. Webb, *Mar. Biol.* **1991**, *109*, 281.

[11] A. P. Lee, L. R. Brooker, D. J. Macey, W. van Bronswijk, J. Webb, *Calcif. Tissue Int.* **2000**, *67*, 408.
[12] J. A. Shaw, D. J. Macey, L. R. Brooker, E. J. Stockdale, M. Saunders, P. L. Clode, *Microsc. Microanal.* **2009**, *15*, 154.
[13] K. S. Kim, D. J. Macey, J. Webb, S. Mann, *Proc. R. Soc. B* **1989**, *237*, 335.
[14] K. M. Towe, *Science* **1963**, *142*, 63.
[15] J. L. Kirschvink, H. A. Lowenstam, *Earth Planet. Sci. Lett.* **1979**, *44*, 193.
[16] K. M. Towe, H. A. Lowenstam, *J. Ultrastruct. Res.* **1967**, *17*, 1.
[17] J. C. Weaver, Q. Wang, A. Miserez, A. Tantuccio, A. Stromberg, K. N. Bozhilov, P. Maxwell, R. Nay, S. T. Heier, E. DiMasi, D. Kisailus, *Mater. Today* **2010**, *13*, 13.
[18] B. A. Wechsler, D. H. Lindsley, C. T. Prewitt, *Am. Mineral.* **1984**, *69*, 754.
[19] K. M. Paralikar, R. H. Balasubramanya, *J. Polym. Sci., Part C: Polym. Lett.* **1984**, *22*, 543.
[20] E. Jansen, A. Kyek, W. Schafer, U. Schwertmann, *Appl. Phys. A: Mater. Sci. Process.* **2002**, *74*, S1004.
[21] P. A. O'Day, N. Rivera, R. Root, S. A. Carroll, *Am. Mineral.* **2004**, *89*, 572.
[22] L. E. Mayhew, S. M. Webb, A. S. Templeton, *Environ. Sci. Technol.* **2011**, *45*, 4468.
[23] L. A. Evans, D. J. Macey, J. Webb, *Calcif. Tissue Int.* **1992**, *51*, 78.
[24] M. K. Jang, B. G. Kong, Y. I. Jeong, C. H. Lee, J. W. Nah, *J. Polym. Sci., Part A: Polym. Chem.* **2004**, *42*, 3423.
[25] H. Ehrlich, *Int. Geol. Rev.* **2010**, *52*, 661.
[26] M. M. Giraudguille, *Tissue Cell* **1984**, *16*, 75.
[27] E. D. Sone, S. Weiner, L. Addadi, *J. Struct. Biol.* **2007**, *158*, 428.
[28] Y. Guyodo, S. K. Banerjee, R. L. Penn, D. Burleson, T. S. Berauo, T. Seda, P. Solheid, *Phys. Earth Planet. Inter.* **2006**, *154*, 222.
[29] R. L. Penn, J. J. Erbs, D. M. Gulliver, *J. Cryst. Growth* **2006**, *293*, 1.
[30] U. Schwertmann, R. M. Cornell, *Iron Oxides in the Laboratory: Preparation and Characterization,* 2nd ed., Wiley-VCH, Weinheim **2000**.
[31] J. G. Stevens, A. M. Khasanov, M. S. G. White, *Hyperfine Interact.* **2003**, *151*, 283.
[32] Z. C. Wu, M. Zhang, K. Yu, S. D. Zhang, Y. Xie, *Chem.–Eur. J.* **2008**, *14*, 5346.
[33] C. F. Baes, R. E. Messmer, *The Hydrolysis of Cations*, John Wiley & Sons, New York **1976**.
[34] M. Mohapatra, T. Padhi, T. Dash, P. Singh, S. Anand, B. K. Mishra, *Toxicol. Environ. Chem.* **2011**, *93*, 844.
[35] U. Schwertmann, J. Friedl, H. Stanjek, *J. Colloid Interface Sci.* **1999**, *209*, 215.
[36] A. Navrotsky, L. Mazeina, J. Majzlan, *Science* **2008**, *319*, 1635.
[37] C. M. Hansel, S. G. Benner, S. Fendorf, *Environ. Sci. Technol.* **2005**, *39*, 7147.
[38] C. M. Hansel, S. G. Benner, J. Neiss, A. Dohnalkova, R. K. Kukkadapu, S. Fendorf, *Geochim. Cosmochim. Acta* **2003**, *67*, 2977.
[39] E. Tronc, P. Belleville, J. P. Jolivet, J. Livage, *Langmuir* **1992**, *8*, 313.
[40] Y. Noguchi, T. Fujiwara, K. Yoshimatsu, Y. Fukumori, *J. Bacteriol.* **1999**, *181*, 2142.
[41] M. Nemoto, Q. Wang, D. Li, S. Pan, T. Matsunaga, D. Kisailus, *Proteomics* **2012**, 1615.
[42] H. J. Choi, S. W. Kang, C. H. Yang, S. G. Rhee, S. E. Ryu, *Nat. Struct. Biol.* **1998**, *5*, 400.
[43] D. Faivre, L. H. Bottger, B. F. Matzanke, D. Schuler, *Angew. Chem., Int. Ed.* **2007**, *46*, 8495.
[44] S. Watanabe, M. Yamanaka, A. Sakai, K. Sawada, T. Iwasa, *Mater. Trans.* **2008**, *49*, 874.
[45] A. Arakaki, J. Webb, T. Matsunaga, *J. Biol. Chem.* **2003**, *278*, 8745.
[46] M. Tanaka, E. Mazuyama, A. Arakaki, T. Matsunaga, *J. Biol. Chem.* **2011**, *286*, 6386.
[47] H. A. Lowenstam, *Geol. Soc. Am. Bull.* **1962**, *73*, 435.
[48] S. M. Webb, *Phys. Scr.* **2005**, *T115*, 1011.